Numerical Investigation of Polymer Exchange Membrane Fuel Cell with Thermal Contact Resistance and Porous Medium Thickness Effect on Temperature Distribution and Performance

Binyamin[1,2] and Ocktaeck Lim[3(✉)]

[1] Graduate School of Mechanical Engineering, University of Ulsan, Ulsan 44610, Republic of Korea
bin279@umkt.ac.id
[2] Department of Mechanical Engineering, Universitas Muhammadiyah Kalimantan Timur, Samarinda, Indonesia
[3] Department of Mechanical Engineering, University of Ulsan, Ulsan 44610, Republic of Korea
otlim@ulsan.ac.kr

Abstract. This study uses a 3-D, isothermal numerical model with isotropic gas diffusion layer (GDL) property to examine how thermal contact resistance (TCR) and porous medium thickness (PMT) between GDL and BP, channel, and various heat transfer coefficients affect the temperature profile and performance of a single PEM fuel cell. The expected plate and cathode electrode temperature changes are compared to experimental findings to calculate the appropriate thermal contact resistance. According to numerical results, TCR and PMT improve cell performance and temperature distribution. 1.5 °C is underestimated by 0.4 V. TCR and PMT affect mass transport and electrode heat. We find that the generated heat cannot be removed entirely when natural air convection is used to cool the PEM fuel cell; however, when liquid water is used, the heat removed ability significantly increases the real expectations of a single PEM fuel cell, and the water must be heated to a proper value that is greater than 70 °C for the cases that were studied. This finding was made after comparing the temperature distribution of various heat transfer coefficients.

Keywords: PEM fuel cell · Temperature distribution · Thermal contact resistance · Porous medium thickness

1 Introduction

Due to energy shortages and fossil fuel pollution, alternative energy sources are essential. Due to its high power density and minimal emissions, the PEM fuel cell has garnered international attention in recent years. PEMFC quickly converts fuel chemical energy into electricity, unlike heat engines. It can generate power at 40–60% efficiency without

T. P. Syawitri et al. (Eds.): MEST 2022, AER 222, pp. 189–209, 2023.
https://doi.org/10.2991/978-94-6463-134-0_19

the Carnot cycle. PEMFC is environmentally safe because it produces just water and heat. PEMFC is a leading choice for distributed power production, portable power sources, and hybrid vehicles due to its benefits [1–3]. PEMFC commercialization requires a model to estimate total performance. Designers can optimize operational settings after assessing PEMFC performance. Fuel cells feature multiple physicochemical processes, which complicates normal modelling. Analytical and mechanistic fuel cell models require knowledge of process parameters and physical phenomena [4].

Based on their simulation, Ge et al. [5] found that the cathode catalyst layer (CCL) reached temperatures 12 degrees Celsius greater than the flow channel. Two-dimensional (2D) models developed by Burheim et al. [6] showed that moisture significantly mitigated the previously observed large temperature difference between the inside and exterior. Cao et al. [7] created 3D models to examine the thermal contact resistance (TCR) between the gas diffusion backer (GDB) and the bipolar plate (BP), which is typically ignored in most studies [6–9]. The data showed that a voltage of 0.6 V was used to estimate a current of 1.5 °C, which was an excess by a factor of 0.3. The transmission of energy via phase change heat and diffusion is typically overlooked in these simplistic models. Common heat-generating sources in PEMFC include the reversible and irreversible heat released by electrode reactions, Joule heating caused by electron/proton conduction, and the phase change heat of water [5]. Energy can be transferred through three different mechanisms: conduction due to a temperature gradient, convection due to the bulk motion of a fluid, and diffusive transport in interdiffusion mixtures [3, 5].

Furthermore, because to the fast changing of loads in the application, automotive PEMFCs are complicated systems. The interior temperature is highly influenced by reaction response time, phase shift, heat conduction, and other factors [13, 14]. As a result, transient models are more precise than steady-state thermal models. However, compared to studies on steady-state heat transfer, those on sudden heat transmission are extremely scarce. In their two-phase, three-dimensional transient model, Wu et al. [13] demonstrated the formation of a “cold spot” at CCL as a result of the evaporation of liquid water. To examine how temperatures evolve during PEMFC startup, Wu et al. [14] employed a quasi-2D numerical model. Most importantly, previous studies often disregarded the thermal contact resistance (TCR) between the GDL and the collector rib. However, a number of studies have shown that contact resistance is an issue that can’t be ignored. The temperature distribution inside a PEMFC was studied by Bapat and Thynell [15], They investigated thermal contact conductance and anisotropic thermal conductivity using a two-dimensional single-phase model. Nitta et al. [16] examined GDL and graphite’s thermal contact resistance, they reported that the bulk resistance of GDL is similar to the contact resistance of GDL and graphite collector throughout a range of compressive pressures. The thermal contact resistance is the principal resistance of the overall thermal resistance, as shown by recent research by Sadeghi et al. [17] into the thermal contact resistance GDL at different compressive pressures.

Within the scope of this research, we make use of a three-dimensional isothermal numerical model that takes into account the fully isotropic properties of the gas diffusion layer to investigate the temperature distribution and the mechanism for heat transfer that takes place within a PEMFC. The optimal values of the PMT and the TCR between

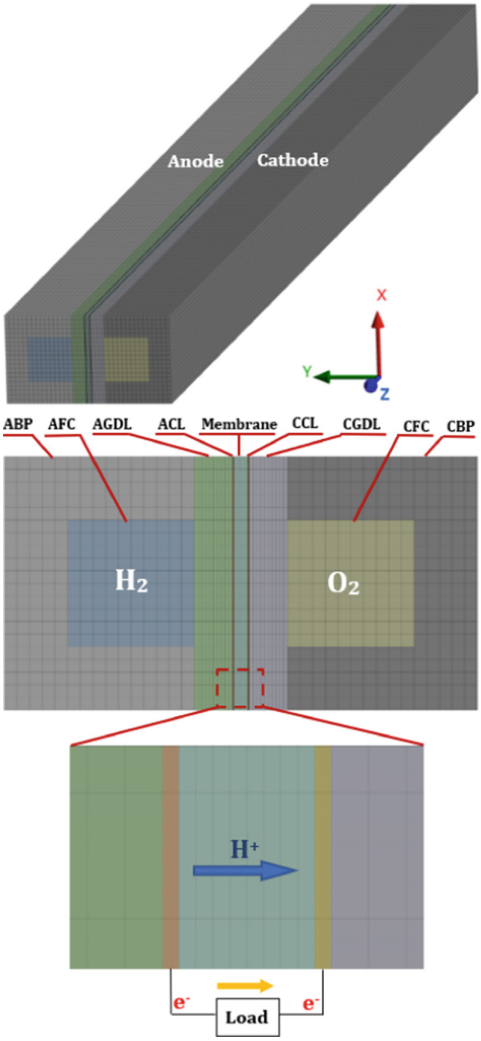

Fig. 1. Diagrammatic representation of the geometry, structure, and computational domain of a single PEMFC cell.

the gas diffusion layer and the current collector rib are determined by comparing the numerically predicted temperature difference between the cathode plate and electrode to the experimental value. This allows for the calculation of the PMT and the TCR between the gas diffusion layer and the current collector rib. After this, subsequent simulations with varying rib and channel widths are performed to analyse channel geometry's effect on the temperature distribution and cell performances.

2 Numerical Model Descriptions

2.1 Assumption

The fuel cell is a complicated system in the process of electrochemical reactions, with numerous factors and surrounding activities influencing the change of fuel cell performance and characteristics. Several hypotheses are developed for the model in order to simplify the equation for simulation analysis.

1. The fuel cell performs in steady-state configuration.
2. All gases are viewed as ideal gases.
3. The fuel cell's flow is laminar.
4. Gases have an incompressible flow.
5. The temperature change is disregarded, and the temperature is fixed at 70°C.
6. All textures in the membrane and GDL are uniformly porous and isotropic.

2.2 Geometric Model

In this section, we create a numerical model of a single-channel PEMFC in three dimensions. The SpaceClaim component constructs the spatial representation. Figure 1 depicts the five components that make up the PEMFC topologies. These components are the proton exchange membrane, the catalyst layers, the gas diffusion layers, the flow channels, and the current collectors. Table 1 summarizes the specific geometric parameters that are consistent with the experimental instance of Wang et al. [18]. The majority of PEMFCs use this design. As a result of its simplicity of design, CFD computation time and effort may be reduced, allowing the task to center on modeling thermal contact resistance with or without its use. If the SIMPLEC solver proves useful for this simple model, it could be expanded to cover more complex PEMFC models. Hydrogen is continuously pumped via the PEM fuel cell's anode flow channel. Hydrogen is converted into protons and electrons at the CL after going through the GDL. Protons from positive hydrogen permeate through the membrane to the cathode, while electrons from the anode move to the related load via the external circuit. The preceding action results in the production of electrical current.

2.3 Conservation Equations

This section provides a brief summary of the numerical model applied for this inquiry. This model is based on a two-phase model created by literatures [22, 23] that can accommodate isotropic transport processes in gas diffusion layers. The cell is believed to be in a steady state, the gas mixing of reacting gas is great, the gas flow is laminar, and the liquid saturation in the gas channel can be disregarded due to the comparatively high velocity in the flow channel. All of these factors point to the cell being in a steady state.

Table 1. Geometric parameters for conventional PEMFC [19].

No.	Parameters	Value (mm)
1	Channel height	1.0
2	Channel width	1.0
3	Channel length	40.0
4	Rib width	1.0
5	Cell width	2.0
6	GDL thickness	0.3
7	CL thickness	0.0129
8	Membrane thickness	0.108

As shown below, a generic convection diffusion equation can explain the conservation equations of momentum, energy, mass, species, and charges.

$$\nabla \bullet (\tilde{\rho} U \phi) = \nabla \bullet \left(\Gamma_\phi \nabla \phi\right) + S_\phi \tag{1}$$

where ϕ is the general variable to be defined, Γ_ϕ is the coefficient of generalized diffusion of ϕ, $\tilde{\rho}$ is the nominal density, and S_ϕ is the variable's source term ϕ. Table 2 lists the expressions of ϕ, $\tilde{\rho}$, and Γ_ϕ for several equations.

Furthermore, the liquid water transport equation in a porous electrode may be expressed as,

$$\nabla \bullet \left(\rho_1 \frac{\eta_g}{\eta_1} \frac{\kappa_{rl}}{\kappa_{rg}} \mathbf{u_g}\right) = \nabla \bullet (\rho_1 D_c \nabla_S) - S_1 \tag{2}$$

where s is the saturation of liquid water and D_c is the diffusivity of s, which is linked to capillary pressure as,

$$D_c = -\frac{KK_1}{\eta_1} \frac{dp_c}{ds} \tag{3}$$

And the expression for dissolved water transport through a membrane is,

$$\nabla \bullet (D_w \nabla C_w) - \nabla \bullet \left(n_d \frac{i}{F}\right) = \mathbf{S_d} \tag{4}$$

where C_w is the water content in the membrane phase, n_d and D_w are the electro-osmotic drag coefficients, and diffusion, respectively.

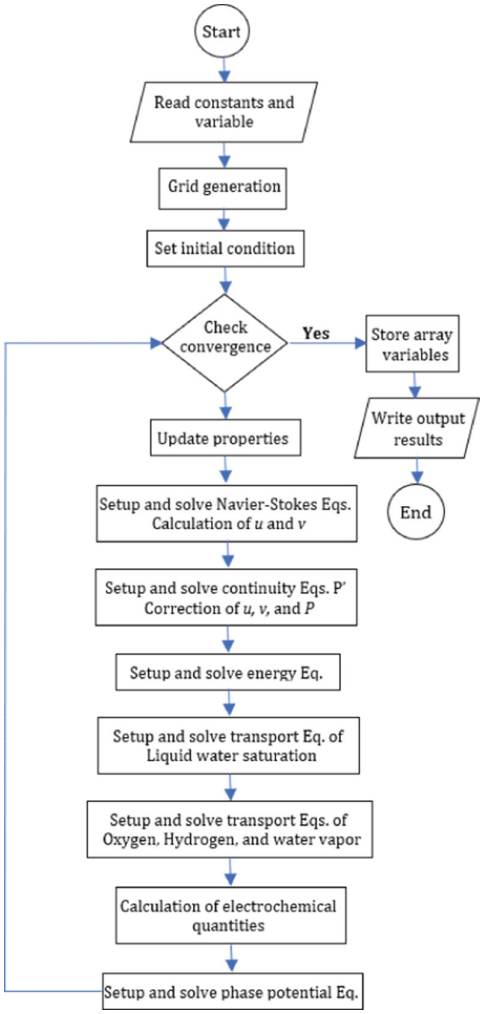

Fig. 2. Algorithm of computational solution

Table 2. ϕ, $\widetilde{\rho}$, $\Gamma_{\varnothing}$ of various governing equations [7].

	Mass	Momentum	Energy	Species	Charges
ϕ	1	U	T	Y_i	φ_s, φ_{mem}
$\widetilde{\rho}$	ρ_{mix}	$\rho_{mix}/\varepsilon_{eff}^2$	ρ_{mix}	ρ_{mix}	0
$\Gamma_{\varnothing}$	0	$\mu_{mix}/\varepsilon_{eff}$	$\frac{\lambda_{eff}}{C_p}$	$\rho_{mix}\, D_i^{eff}$	σ_{sol}, σ_{mem}

2.4 Boundary Condition and Numerical Procedure

Mass-flow inlet and pressure outlet describe the input and output boundaries of the channel, respectively. Use this formula to get the inlet velocities [19]:

$$u_a^{in} = \zeta_a \frac{i_{max}}{2F} A_{MEA} \frac{1}{\omega_{H_2}^{in}} \frac{RT_a^{in}}{p_a^{in}} \frac{1}{A_{ch}} \tag{5}$$

$$u_c^{in} = \zeta_c \frac{i_{max}}{4F} A_{MEA} \frac{1}{\omega_{O_2}^{in}} \frac{RT_c^{in}}{p_c^{in}} \frac{1}{A_{ch}} \tag{6}$$

where ζ is the ratio of stoichiometric, F is the Faraday constant (96,487 °C mol^{-1}), R is the gas constant (8,314 J mol-1 K), and i_{max} is the maximum average of current density, respectively. A_{MEA} and A_{ch} represent the geometrical area of the MEA and the cross-sectional area of the channel, respectively. ω is the mass fraction of the inlet species, which may be determined by using the inlet temperature T, pressure p, and relative humidity RH. At the inlet border, in addition to the inlet velocity, here are the values reported for the gas mixture's temperature and mass fraction:

$$Y_{H_2} = Y_{H_2,in}, Y_{O_2} = Y_{O_2,in}, Y_{H_2O} = Y_{H_2O,in}, T_{in} = T_{cell} \tag{7}$$

where $YH_{2,in}$, $YO_{2,in}$, and $YH_2O_{,in}$ can be easily determined using the molar fraction, and the water vapor molar fraction, XH_2O; may be calculated from the gas inlet humidity as,

$$X_{H_2O,a} = \frac{RH_a P_{sat}}{P_a}, X_{H_2O,c} = \frac{RH_c P_{sat}}{P_c} \tag{8}$$

The molar fraction of hydrogen, XH_2, and molar fraction of oxygen, XO_2, are then computed since pure hydrogen and oxygen are utilized.

$$X_{H_2} = 1 - X_{H_2O,a}, X_{O_2} = 1 - X_{H_2O,c}, \tag{9}$$

Gas outlet: At the outlet boundary, the fully matured assumption is used [22].

$$\frac{\partial \phi}{\partial X} = 0 \tag{10}$$

Anode and cathode outer surface: As given in Fig. 1, for electron transmission, the anode and cathode outer surfaces are connected to the outer circuit. The temperature and electronic potential are set in step one.

$$\varphi_{s,a} = 0, \varphi_{s,c} = V_{cell}, T = T_w = T_{cell} \tag{11}$$

The adiabatic condition is used for the protonic potential,

$$\frac{\partial \varphi_m}{\partial Z} = 0 \tag{12}$$

Periodic structure across y-direction: The symmetry requirement is used at the surface of the y-outer direction because the structure along y-direction is periodic.

$$v = 0, \frac{\partial u}{\partial y} = 0, \frac{\partial W}{\partial y} = 0, \frac{\partial \phi}{\partial y} = 0 \tag{13}$$

Table 3. Complementary equation and definitions.

Parameters	Expressions
GDL intrinsic permeability [23]	$\frac{K}{R^2} = \frac{\varepsilon(\varepsilon-\varepsilon_p)^{\alpha+2}}{8(\ln\varepsilon)^2(1-\varepsilon)^{\alpha}[(\alpha+1)\varepsilon-\varepsilon_p]^2}$
Coefficient of GDL effective mass diffusion [26, 27]	$D_{\text{eff}} = f(\varepsilon)D_{i,bulk}, D_{i,bulk} = D_i^0(p_0/p)^{1.0}(T/T_0)^{1.5}$, Through plane: $f(\varepsilon)_{th} = 1 - 2.76\varepsilon\cosh(3\varepsilon - 1.92)[3(1-\varepsilon)/(3-\varepsilon)]$, In plane: $f(\varepsilon)_{in} = 1 - 1.72\varepsilon\cosh(2.07\varepsilon - 2.11)[3(1-\varepsilon)/(3-\varepsilon)]$
GDL effective thermal conductivity [26]	Through plane: $k_{eff}^{th}/k_s =$ $1 - 0.963(1-\varepsilon)^{-0.008}\exp[0.881(1-\varepsilon)][3\varepsilon/(3-(1-\varepsilon))]$, In plane: $k_{eff}^{th}/k_s =$ $1 - 0.977(1-\varepsilon)^{-0.009}\exp[0.344(1-\varepsilon)][3\varepsilon/(3-(1-\varepsilon))]$
Electrochemical kinetics [21, 27]	$R_{\text{a}} = \theta A_s i_{\text{a,ref}}\left(\frac{C_h}{C_{\text{h,ref}}}\right)^{1/2}\left\{\exp\left[\frac{\alpha_{\text{a}}F}{RT}\eta_{\text{a}}\right] - \exp\left[-\frac{(1-\alpha_{\text{a}})F}{RT}\eta_{\text{a}}\right]\right\}$ $R_{\text{c}} = \theta A_s i_{\text{c,ref}}\frac{C_o}{C_{\text{o,ref}}}\left\{\exp\left[\frac{\alpha_{\text{c}}F}{RT}\eta_{\text{c}}\right] - \exp\left[-\frac{(1-\alpha_{\text{c}})F}{RT}\eta_{\text{c}}\right]\right\}$
Over-potential	$\eta_{\text{a}} = \phi_{\text{s}} - \phi_{\text{m}}, \eta_{\text{c}} = V_{\text{oc}} - \phi_{\text{s}} + \phi_{\text{m}}$
Open circuit voltage [21]	$V_{\text{oc}} = 1.23 - 0.9\times10^{-3} + 2.3\frac{RT}{4F}\log\left(p_a^2 p_c\right)$
Membrane electrical conductivity [28]	$\sigma_{\text{mem}} = (0.5193 - 0.326)\exp\left[1268\left(\frac{1}{303} - \frac{1}{T}\right)\right]$
GDL effective electrical conductivity [28]	Through plane: $\sigma_{eff}^{th}/k_s =$ $1 - 0.962(1-\varepsilon)^{-0.007}\exp[0.889(1-\varepsilon)][3\varepsilon/(3-(1-\varepsilon))]$, In plane: $\sigma_{eff}^{th}/\sigma_s =$ $1 - 0.962(1-\varepsilon)^{-0.016}\exp[0.367(1-\varepsilon)][3\varepsilon/(3-(1-\varepsilon))]$
Capillary pressure [29]	$p_{\text{c}} = \left(\frac{\varepsilon}{K}\right)^{0.5}\sigma J(s), J(s) =$ $\begin{cases}\cos\theta_{\text{c}}\left[1.417(1-s) - 2.212(1-s)^2 + 1.236(1-s)^3\right]\theta_{\text{c}} < 90^\circ \\ \cos\theta_{\text{c}}\left[1.417s - 2.212s^2 + 1.236s^3\right]\theta_{\text{c}} > 90^\circ\end{cases}$
Water saturation pressure [21]	$Log_{10}P_{sat} =$ $-2.1794 + 0.02953T - 9.1837\times10^{-5}T^2 + 1.4454\times10^{-7}T^3$
Relative permeability [21]	$K_{rl} = S^3, K_{rg} = (1-S)^3$

(*continued*)

Table 3. (*continued*)

Parameters	Expressions
Membrane water diffusion coefficient [28]	$D_w = 2.1 \times 10^{-7} \exp(-2346/T) C_w$
Coefficient of electro-osmotic drag [30]	$n_d = \frac{2.5}{22}$
Equilibrium membrane water content [30]	$_e = \begin{cases} 1.41 + 22.3a_{H_2O} - 18.8a_{H_2O}^2 - 16.2a_{H_2O}^3, 0 \le a_{H_2O} \le 1 \\ 10.1 + 2.94(a_{H_2O} - 1) 1 < a_{H_2O} \le 3 \end{cases}$
Wate vapor activity [30]	$a_{H_2O} = \frac{x_w p}{p_{\text{sat}}} + 2s$

2.5 Grid Independent Test and Validation Model

To solve the aforesaid problem, an in-house computer algorithm based on the finite volume approach is applied. Because of the wide variance in thickness of various layers, a hexahedral grid is employed in the Z direction, while uniform grids are utilized in the X and Y directions, as shown in This section provides a brief summary of the numerical model applied for this inquiry. This model is based on a two-phase model created by literatures [22, 23] that can accommodate isotropic transport processes in gas diffusion layers. The cell is believed to be in a steady state, the gas mixing of reacting gas is great, the gas flow is laminar, and the liquid saturation in the gas channel can be disregarded due to the comparatively high velocity in the flow channel. All of these factors point to the cell being in a steady state (Table 4).

The grid independence test is carried out using five alternative grid systems. The quantity of five grids is 496,000, 512,000, 544,000, 560,000 and 592,000 respectively, as findings are described in Table 6. Finally, taking into account the balance of precision and economics grid system is used in this work. The solid walls are believed to have zero fluxes and no slide. The potential is 0 V at the anode terminal. There is a 0.90 V to 0.40 V spread (within a 0.05 V range) at the cathode terminal. Pressure-velocity coupling is solved using the SIMPLEC algorithm, and interpolation functions are calculated using the second-order upwind method. In contrast to the more relaxed convergence criterion of 10E-3 for the other equations, the energy equation requires a value of 10E-6 for convergence. Table 5 summarizes the specifics of the operational settings (Fig. 3).

Table 4. Governing equation of source term in different region [31].

Equation	Source terms
Mass	In GDL: $S_{\mathrm{m}} = S_{\mathrm{h}} + S_0 + S_{\mathrm{w}}$, lnCL : $S_{\mathrm{m}} = S_{\mathrm{t}}$
Momentum	In GDL: CL : $S_u = -\frac{\mu_{\mathrm{g}} \mathbf{u}_{\mathrm{g}}}{KK_{rg}} - \nabla p_{\mathrm{g}}$, In GC: $S_u = -\nabla p_{\mathrm{g}}$
Species	In ACL: $S_{\mathrm{h}} = -\left(\frac{R_{\mathrm{a}}}{2F}\right) M_{\mathrm{h}}$, InCCL : $S_{\mathrm{O}} = -\left(\frac{R_{\mathrm{c}}}{4F}\right) M_{\mathrm{O}}$
Potential	In CL: $S_{\mathrm{w}} = -\left(\frac{R_{\mathrm{c}}}{2F}\right) M_{\mathrm{w}} + S_{\mathrm{d}} + S_{\mathrm{l}}$, InGDL : $S_{\mathrm{w}} = S_l$ In ACL: $S_{\phi,\mathrm{s}} = -R_{\mathrm{a}}$, InCCL : $S_{\phi,\mathrm{s}} = -R_c$
Energy	In CL: $S_T = i\left(\eta + T\frac{dE}{dT}\right) + \frac{I^2}{\sigma_s} + S_l h_{fg}$, InGDL : $S_T = \frac{I^2}{\sigma_s} + S_l h_{fg}$, InMEM : $S_T = \frac{I^2}{\sigma_{\mathrm{mem}}}$
Liquid saturation	In CL: GDL: $S_l = A_{pore}\frac{Sh_{\mathrm{c}} D_w}{\bar{d}}(1-s)(\rho_w - \rho_{sat})q + A_{pore}\frac{Sh_{\mathrm{c}} D_w}{\bar{d}} s(\rho_w - \rho_{sat})(1-q)$
Dissolved water	In ACL: $S_{\mathrm{d,a}} = -\gamma_a\left(C_{\mathrm{w,a}} - a^*_{w,a}\right)$ In CCL: $S_{\mathrm{d,c}} = -\gamma_d\left(C_{\mathrm{w,c}} - a^*_{w,c}\right) + R_{\mathrm{c}}/2F$

To validate the computational model findings, the simulated polarization curves are compared with experimental and simulation data from Wang et al. [18] and Li et al. [19], as shown in Fig. 2. For model validation, four operating conditions at varying operating temperatures and pressures are employed. Table 3 lists the other operational parameters utilized to produce the polarization curves. The model is validated by confirming that the findings of three polarization curves under varying operational conditions are in reasonable agreement with those of the experiments. It's worth noticing that the model outperforms the experiments when the current density is large. This is due to the fact that the CFD analysis relied on a single-phase model, which has its own shortcomings when applied to estimating PEM fuel cell performance under high current density.

Table 5. Operating parameters for validation [19].

No.	Parameters	Value
1	Operating pressure	1 atm
2	Operating temperature	70 °C
3	Open-circuit voltage	0.95 V
4	Cathode reference current density	5210 A m^{-2}
5	Anode reference current density	9×10^8 A m^{-2}
6	Relative humidity of inlet gases	100%
7	Anode fuel	H_2 (20%) and H_2O (80%)
8	Cathode fuel	O_2 (18.5%) and H_2O (22%)
9	GDL porosity	0.4
10	CL porosity	0.5
11	Membrane porosity	0.25
12	Ratio of anode stoichiometric	3
13	Ratio of Cathode stoichiometric	3
14	H_2 reference concentration	54.7 mol m^{-3}
15	O_2 reference concentration	3.39 mol m^{-3}
16	Anode concentration exponent	0.5
17	Cathode concentration exponent	1
18	H_2 reference diffusivity	3.9×10^{-5} m^2 s^{-1}
19	O_2 reference diffusivity	2.275×10^{-5} m^2 s^{-1}
20	H_2O reference diffusivity	3.9×10^{-5} m^2 s^{-1}
21	Other species reference diffusivity	5.2×10^{-5} m^2 s^{-1}

Table 6. Grid independence test results.

No.	Grid number	Average current density/ A cm^{-2} ($V_{cell} = 0.60$ V)	Time consumed for 100 iteration (s)
1	496,000	0.74918	758
2	512,000	0.76787	792
3	544,000	0.72785	1052
4	560,000	0.75763	1102
5	592,000	0.73686	1193

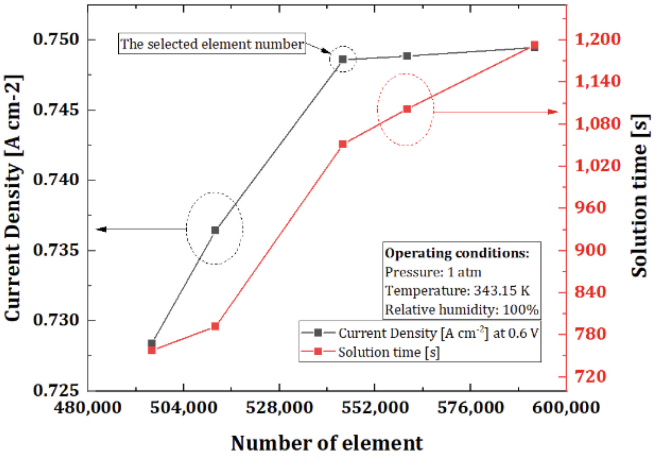

(a)

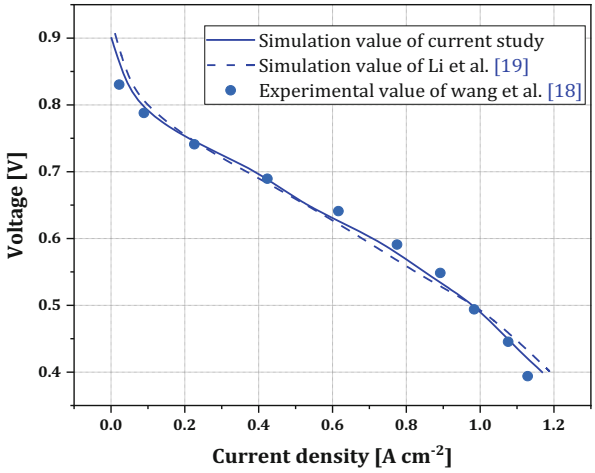

(b)

Fig. 3. (a) Grid independency test for the current density at V = 0.60 V, (b) The polarization curves comparison between numerical results of present study with simulation [19] and experiment values [18].

3 Results and Discussion

In this part, the temperature distribution in the PEMFC is carefully analyzed using numerical findings under different operating situations. First, we discuss how the heat transfer process is affected by the contact resistance and porous medium thickness between the GDL and the collector rib. Next, we look into how changing the width of the channels or the ratio of ribs to channels affects the efficiency of the cells. The final section presents temperature distributions under various heat dissipation scenarios.

3.1 The Influence of Thermal Contact Resistance and Porous Medium Thickness on Temperature Gradient

PEMFC contact surfaces have thermal contact resistance and porous medium thickness. Because the MEA is usually created using a hot press technique, it is often thought that the contact resistance between the GDL and catalyst coated membrane (CCM) is modest enough to ignore and only the contact resistance and porous medium thickness between the GDL and collector are considered. According to Nitta et al. [16], GDL and graphite collector thermal contact resistance ranges from 0.3 to 22.5 $\times$ 10^{-4} m^2 KW^{-1} under varied compression pressures. Sadeghifar et al. [32] found that the thermal contact resistance between GDL and iron surface ranges from 1.0 $\times$ 10^{-4} m^2 KW^{-1} and 8.0 $\times$ 10^{-4} m^2 KW^{-1} depending on the type of GDL and compression force. This study measured GDL-collector thermal contact resistance from 0 to 3.75 $\times$ 10^{-4} m^2 KW^{-1}. Figure 4 shows temperature distributions without thermal contact resistances

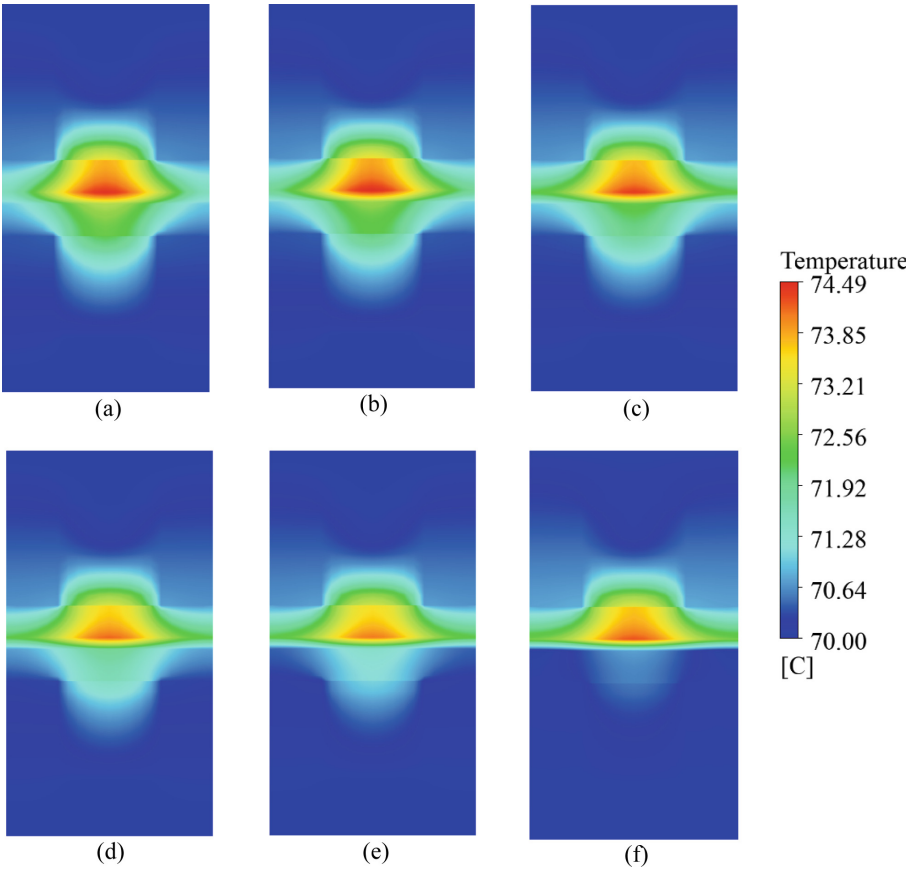

Fig. 4. Temperature distributions at plane-xy with different cell voltages (a) 0.4 V, (b) 0.5 V, (c) 0.6 V, (d) 0.7 V, (e) 0.8 V, and (f) 0.9 V without considering TCR and PMT (operating temperature, T = 70 °C; operating pressure, P = 1 atm; anode gas: hydrogen; cathode gas: oxygen).

and Fig. 5 with thermal contact resistances and porous medium thickness for output voltages from 0.4 to 0.9 V. The channel temperature rises with distance from the rib. Since porous GDL has a very low velocity, heat conduction removes electrode heat from the rib region. Additionally, TCR and PMT values raise maximum cell temperature. TCR and PMT between the GDL and collector rib enhance heat transfer resistance and make porous electrode heat dissipation harder. As TCR and PMT grow, the current collector temperature becomes more uniform and the temperature decrease across the GDL/collector rib increases. The TCR and PMT prevent heat dissipation.

Figure 4 illustrates temperature profiles with and without TCR and PMT at the XY-Plane along the Y-Axis. The oxygen reduction process generates most of the heat, therefore the highest temperature lies near the cathode catalyst layer. As the output cell voltage lowers, the cell generates more heat, raising the maximum temperature. Figure 5 shows how TCR affects PEMFC temperature profile. Ignoring the TCR and PMT can lower the MEA's temperature. The highest temperature difference between these two

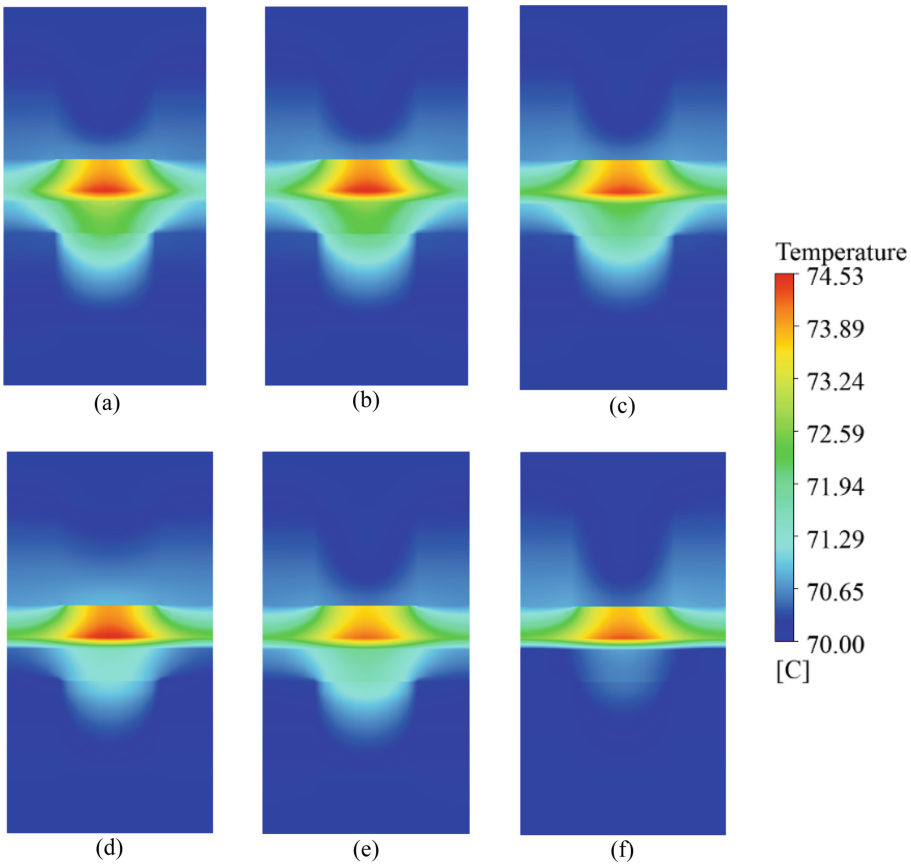

Fig. 5. Temperature distributions at plane-xy with different cell voltages (a) 0.4 V, (b) 0.5 V, (c) 0.6 V, (d) 0.7 V, (e) 0.8 V, and (f) 0.9 V with considering TCR and PMT (operating temperature, T = 70 °C; operating pressure, P = 1 atm; anode gas: hydrogen; cathode gas: oxygen).

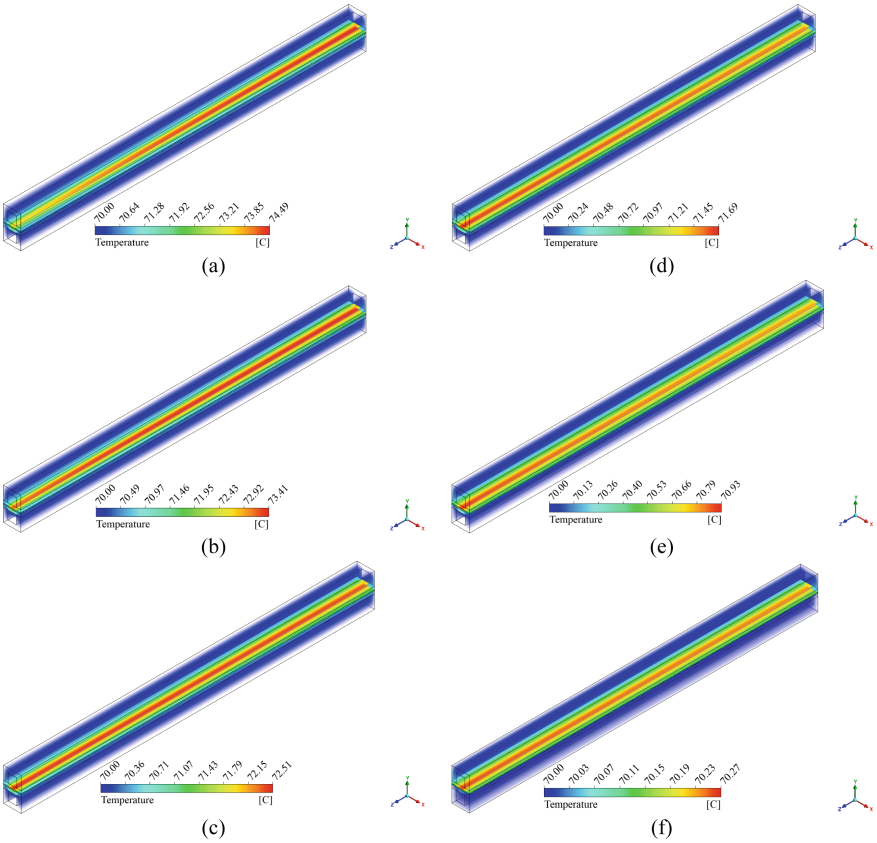

Fig. 6. Temperature distributions at isoview with different cell voltages (a) 0.4 V, (b) 0.5 V, (c) 0.6 V, (d) 0.7 V, (e) 0.8 V, and (f) 0.9 V without considering TCR and PMT (operating temperature, T = 70 °C; operating pressure, P = 1 atm; anode gas: hydrogen; cathode gas: oxygen).

scenarios is 1.5 °C when the output cell voltage is 0.4 V, and it climbs to 0.5 °C when the cell voltage is 0.4 V. Figure 6 shows an iso-volume temperature distribution without TCR or PMT. Finally, the MEA temperature profile differs between Fig. 8(a) and Fig (b). Figures 8(a) and 8(b) show MEA's "Λ" temperature profile (b). TCR and PMT between collector rib and GDL create all motion phenomena. The TCR and PMT between the rib and the GDL hinder heat dissipation, raising MEA temperature (Figs. 7 and 9).

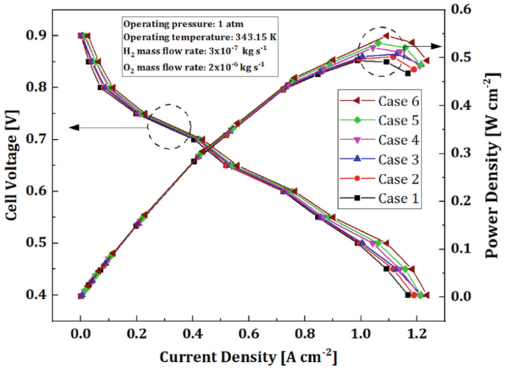

Fig. 7. Polarization curve and power density of difference cases (operating temperature, T = 70 °C; operating pressure = 1 atm, H_2 mass flow-rate: 3×10^{-7} kg s^{-1}, O_2 mass flow-rate: 2×10^{-6} kg s^{-1})

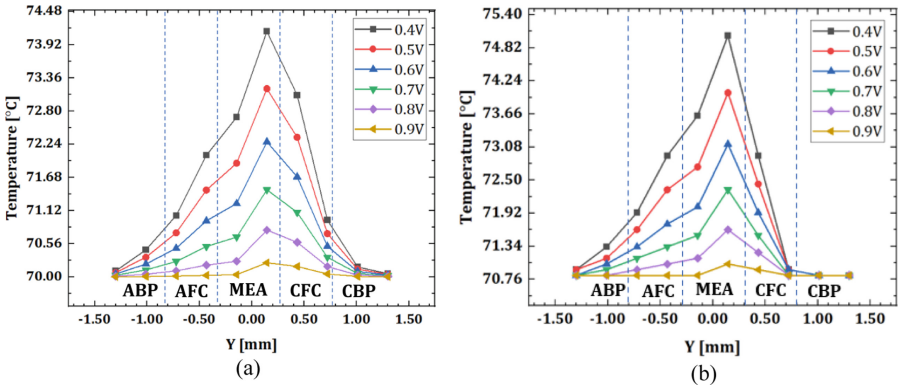

Fig. 8. Temperature profiles along Y-axis with different cell output voltage: (a) without (b) with TCR and PMT

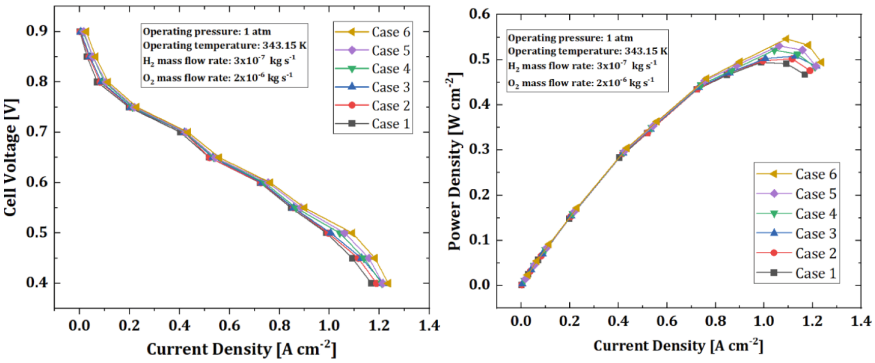

Fig. 9. (a) Polarization and (b) power density curves with various cases (operating temperature, T = 70 °C; operating pressure = 1 atm, H_2 mass flow-rate: 3×10^{-7} kg s^{-1}, O_2 mass flow-rate: 2×10^{-6} kg s^{-1}).

3.2 Water Mass Fraction

Figure 10 displays the iso-volume of water mass fraction profile for six distinct cell voltages. At 0.4 V cell voltage, water saturation is lower and current density is higher. The porous electrode heats up to a higher temperature in both the TCR and PMT scenarios, as shown in Fig. 6. As the electrode temperature rises, less water vapor condenses into liquid water due to an increase in the water saturation pressure. This explains why PMT and TCR have lower saturation. Additionally, rising temperature encourages electrochemical processes and transports oxygen through the GDL to the reaction site; likewise, falling liquid water saturation in the case of TCR and PMT enhances oxygen transport. These advantages contribute to enhanced cell performance in TCR and PMT conditions.

3.3 Pressure Drops

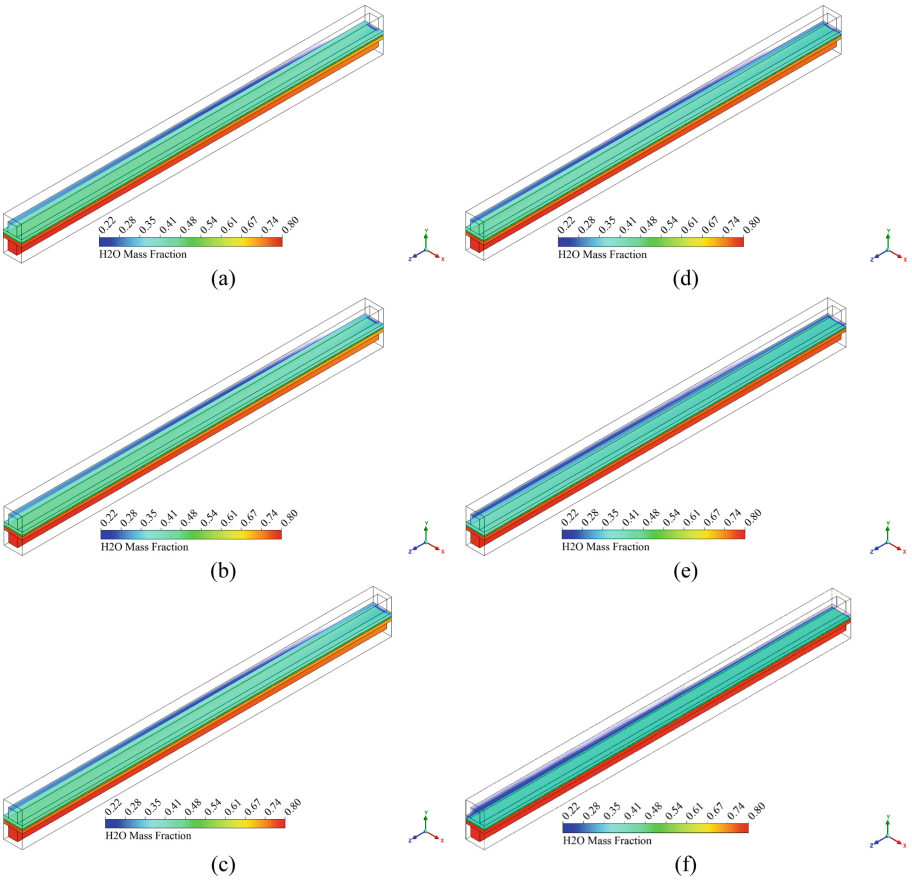

Fig. 10. Iso-volume profiles of H_2O mass fraction within the fuel cell without considering TCR and PMT with different cell voltages (a) 0.4 V, (b) 0.5 V, (c) 0.6 V, (d) 0.7 V, (e) 0.8 V, and (f) 0.9 V.

4 Conclusions

In this research, we employed a numerical model of an isothermal fuel cell to examine the temperature distribution of PEM fuel cells taking into account the impacts of temperature coefficient of resistance (TCR) and potential mobility transition (PMT). The model's TCR and PMT were fine-tuned by comparing simulated and experimental findings for temperature changes between the flow plate and the cathode electrode. The impact of channel and rib widths, in addition to various cooling strategies, on heat dissipation and PEM fuel cell performance was then investigated using numerical models in conjunction with defined TCR and PMT. The numerical results and the explanation in the previous section lead to the following inferences:

(1) The TCR and PMT have an effect that can't be disregarded if we want to make better predictions about cell performance and temperature distribution. The precise

values of TCR and PMT for case 6 were calculated to be 0.1 m^2 K W^{-1} and 3.5 × 10^{-5} m.

(2) Both the peak and average temperatures inside the electrode are influenced by TCR and PMT. Maximum cell temperature is underestimated by roughly 1.5 °C at 0.4 V when the TCR and PMT are disregarded, and the temperature profile takes on a "Λ" shape.

(3) The numerical investigations here, which take into account the TCR and the PMT, are beneficial to oxygen transport and water removal and favour the uniform distribution of oxygen and current densities within fuel cells. Furthermore, taking into account the TCR and the PMT tends to reduce the dissolved water content within the cathode catalyst layer and improve cell performance.

Acknowledgement. This work was supported by the Technology Innovation Program (or Industrial Strategic Technology Development Program-The technology development on fuel cell electric propulsion system using Land Based Test Site) (RS-2022-00142947, The technology development on fuel cell electric propulsion system using Land Based Test Site) funded By the Ministry of Trade, Industry & Energy (MOTIE, Korea).

References

1. D. Zhou, A. Al-durra, F. Gao, A. Ravey, I. Matraji, and M. Godoy, "Online energy management strategy of fuel cell hybrid electric vehicles based on data fusion approach," vol. 366, pp. 278–291, 2017, https://doi.org/10.1016/j.jpowsour.2017.08.107.
2. J. P. Stempien and S. H. Chan, "Comparative study of fuel cell , battery and hybrid buses for renewable energy constrained areas," J. Power Sources, vol. 340, pp. 347–355, 2017, https://doi.org/10.1016/j.jpowsour.2016.11.089.
3. A. Kosakian, L. P. Urbina, A. Heaman, and M. Secanell, "Electrochimica Acta Understanding single-phase water-management signatures in fuel- cell impedance spectra : A numerical study," Electrochim. Acta, vol. 350, p. 136204, 2020, https://doi.org/10.1016/j.electacta.2020.136204.
4. Q. Wang et al., "Numerical analysis of static and dynamic heat transfer behaviors inside proton exchange membrane fuel cell," J. Power Sources, vol. 488, no. December 2020, p. 229419, 2021, https://doi.org/10.1016/j.jpowsour.2020.229419.
5. N. Ge et al., "International Journal of Heat and Mass Transfer Non-isothermal two-phase transport in a polymer electrolyte membrane fuel cell with crack-free microporous layers," Int. J. Heat Mass Transf., vol. 107, pp. 418–431, 2017, https://doi.org/10.1016/j.ijheatmasstransfer.2016.11.045.
6. E. C. S. Transactions and T. E. Society, "Thermal Gradients and Thermal Conductivity in PEM Fuel Cells, Compared to Li-ion Batteries and Super Capacitors Odne S. Burheim," vol. 86, no. 13, pp. 97–109, 2018.
7. T. Cao, Y. Mu, J. Ding, H. Lin, Y. He, and W. Tao, "International Journal of Heat and Mass Transfer Modeling the temperature distribution and performance of a PEM fuel cell with thermal contact resistance," Int. J. Heat Mass Transf., vol. 87, pp. 544–556, 2015, https://doi.org/10.1016/j.ijheatmasstransfer.2015.04.010.

8. L. Xing, S. Du, R. Chen, M. Mamlouk, and K. Scott, "Anode partial fl ooding modelling of proton exchange membrane fuel cells : Model development and validation," Energy, vol. 96, pp. 80–95, 2016, https://doi.org/10.1016/j.energy.2015.12.048.
9. M. Bhaiya, A. Putz, and M. Secanell, "Electrochimica Acta Analysis of non-isothermal effects on polymer electrolyte fuel cell electrode assemblies," Electrochim. Acta, vol. 147, pp. 294–309, 2014, https://doi.org/10.1016/j.electacta.2014.09.051.
10. J. Song, Y. Huang, J. Zeng, L. Chen, and Y. Wu, "Design and numerical investigation of multi-channel cooling plate for proton exchange membrane fuel cell," Energy Reports, vol. 8, pp. 6058–6067, 2022, https://doi.org/10.1016/j.egyr.2022.04.052.
11. S. Islam, "Modeling and Control of Fuel Cell Power System with Varying Load and," pp. 1236–1241, 2020.
12. A. Goshtasbi, B. L. Pence, and T. Ersal, "Computationally Efficient Pseudo-2D Non-Isothermal Modeling of Polymer Electrolyte Membrane Fuel Cells with Two-Phase Phenomena," vol. 163, no. 13, pp. 24–26, 2016, https://doi.org/10.1149/2.0871613jes.
13. H. Wu, P. Berg, and X. Li, "Modeling of PEMFC Transients with Finite-Rate Phase-Transfer Processes," J. Electrochem. Soc., vol. 157, no. 1, p. B1, Nov. 2010, https://doi.org/10.1149/1.3248005/XML.
14. K. Wu, K. Jiao, and B. Zu, "A Quasi-2D Transient Multiphase Modeling of Cold Start Processes in Proton Exchange Membrane Fuel Cell," SAE Tech. Pap., vol. 2019-April, no. April, Apr. 2019, https://doi.org/10.4271/2019-01-0390.
15. C. J. Bapat and S. T. Thynell, "Anisotropic heat conduction effects in proton-exchange membrane fuel cells," J. Heat Transfer, vol. 129, no. 9, pp. 1109–1118, 2007, https://doi.org/10.1115/1.2712478.
16. I. Nitta, O. Himanen, and M. Mikkola, "Thermal Conductivity and Contact Resistance of Compressed Gas Diffusion Layer of PEM Fuel Cell," Fuel Cells, vol. 8, no. 2, pp. 111–119, Apr. 2008, https://doi.org/10.1002/FUCE.200700054.
17. E. Sadeghi, N. Djilali, and M. Bahrami, "Effective thermal conductivity and thermal contact resistance of gas diffusion layers in proton exchange membrane fuel cells. Part 1: Effect of compressive load," J. Power Sources, vol. 196, no. 1, pp. 246–254, 2011, https://doi.org/10.1016/j.jpowsour.2010.06.039.
18. L. Wang, A. Husar, T. Zhou, and H. Liu, "A parametric study of PEM fuel cell performances," Int. J. Hydrogen Energy, vol. 28, no. 11, pp. 1263–1272, 2003, https://doi.org/10.1016/S0360-3199(02)00284-7.
19. H. Li, B. Xu, C. Du, and Y. Yang, "Performance prediction and power density maximization of a proton exchange membrane fuel cell based on deep belief network," J. Power Sources, vol. 461, no. March, p. 228154, 2020, https://doi.org/10.1016/j.jpowsour.2020.228154.
20. C. H. Min, Y. L. He, X. L. Liu, B. H. Yin, W. Jiang, and W. Q. Tao, "Parameter sensitivity examination and discussion of PEM fuel cell simulation model validation. Part II: Results of sensitivity analysis and validation of the model," J. Power Sources, vol. 160, no. 1, pp. 374–385, 2006, https://doi.org/10.1016/j.jpowsour.2006.01.080.
21. W. Q. Tao, C. H. Min, X. L. Liu, Y. L. He, B. H. Yin, and W. Jiang, "Parameter sensitivity examination and discussion of PEM fuel cell simulation model validation. Part I. Current status of modeling research and model development," J. Power Sources, vol. 160, no. 1, pp. 359–373, 2006, https://doi.org/10.1016/j.jpowsour.2006.01.078.
22. S. V. Patankar, "Numerical Heat Transfer and Fluid Flow," Oct. 2018, https://doi.org/10.1201/9781482234213.
23. M. M. Tomadakis and T. J. Robertson, "Viscous Permeability of Random Fiber Structures: Comparison of Electrical and Diffusional Estimates with Experimental and Analytical Results," https://doi.org/10.1177/0021998305046438, vol. 39, no. 2, pp. 163–188, Jul. 2016, https://doi.org/10.1177/0021998305046438.

24. T. Berning, D. M. Lu, and N. Djilali, "Three-dimensional computational analysis of transport phenomena in a PEM fuel cell," J. Power Sources, vol. 106, no. 1–2, pp. 284–294, 2002, https://doi.org/10.1016/S0378-7753(01)01057-6.
25. N. Zamel, X. Li, and J. Shen, "Correlation for the effective gas diffusion coefficient in carbon paper diffusion media," Energy and Fuels, vol. 23, no. 12, pp. 6070–6078, 2009, https://doi.org/10.1021/ef900653x.
26. N. Zamel, X. Li, J. Shen, J. Becker, and A. Wiegmann, "Estimating effective thermal conductivity in carbon paper diffusion media," Chem. Eng. Sci., vol. 65, no. 13, pp. 3994–4006, 2010, https://doi.org/10.1016/j.ces.2010.03.047.
27. X. Liu, W. Tao, Z. Li, and Y. He, "Three-dimensional transport model of PEM fuel cell with straight flow channels," J. Power Sources, vol. 158, pp. 25–35, 2006, https://doi.org/10.1016/j.jpowsour.2005.08.046.
28. T. E. Springer, T. A. Zawodzinski, and S. Gottesfeld, "Polymer Electrolyte Fuel Cell Model," J. Electrochem. Soc., vol. 138, no. 8, pp. 2334–2342, Aug. 1991, https://doi.org/10.1149/1.2085971/XML.
29. Y. Wang and C.-Y. Wang, "A Nonisothermal, Two-Phase Model for Polymer Electrolyte Fuel Cells," J. Electrochem. Soc., vol. 153, no. 6, p. A1193, Apr. 2006, https://doi.org/10.1149/1.2193403/XML.
30. Q. Ye and T. Van Nguyen, "Three-Dimensional Simulation of Liquid Water Distribution in a PEMFC with Experimentally Measured Capillary Functions," J. Electrochem. Soc., vol. 154, no. 12, p. B1242, Oct. 2007, https://doi.org/10.1149/1.2783775/XML.
31. T. F. Cao, H. Lin, L. Chen, Y. L. He, and W. Q. Tao, "Numerical investigation of the coupled water and thermal management in PEM fuel cell," Appl. Energy, vol. 112, pp. 1115–1125, 2013, https://doi.org/10.1016/j.apenergy.2013.02.031.
32. H. Sadeghifar, N. Djilali, and M. Bahrami, "Effect of Polytetrafluoroethylene (PTFE) and micro porous layer (MPL) on thermal conductivity of fuel cell gas diffusion layers: Modeling and experiments," J. Power Sources, vol. 248, pp. 632–641, 2014, https://doi.org/10.1016/J.JPOWSOUR.2013.09.136.